



HAL
open science

On the role of viscoelasticity in mucociliary clearance: a hydrodynamic continuum approach

Anjishnu Choudhury, Marcel Filoche, Neil Ribe, Nicolas Grenier, Georg F. Dietze

► To cite this version:

Anjishnu Choudhury, Marcel Filoche, Neil Ribe, Nicolas Grenier, Georg F. Dietze. On the role of viscoelasticity in mucociliary clearance: a hydrodynamic continuum approach. *Journal of Fluid Mechanics*, 2023, 971, pp.A33. 10.1017/jfm.2023.682 . hal-04304427

HAL Id: hal-04304427

<https://hal.science/hal-04304427v1>

Submitted on 24 Nov 2023

HAL is a multi-disciplinary open access archive for the deposit and dissemination of scientific research documents, whether they are published or not. The documents may come from teaching and research institutions in France or abroad, or from public or private research centers.

L'archive ouverte pluridisciplinaire **HAL**, est destinée au dépôt et à la diffusion de documents scientifiques de niveau recherche, publiés ou non, émanant des établissements d'enseignement et de recherche français ou étrangers, des laboratoires publics ou privés.

Banner appropriate to article type will appear here in typeset article

On the role of viscoelasticity in mucociliary clearance: a hydrodynamic continuum approach

A. Choudhury¹†, M. Filoche^{2,3}, N. M. Ribe¹, N. Grenier⁴ and G. F. Dietze¹

¹Université Paris-Saclay, CNRS, FAST, 91405, Orsay, France.

²Institut Langevin, ESPCI Paris, Université PSL, CNRS, 75005 Paris, France

³Institut Mondor de Recherche Biomédicale, INSERM-UPEC, CNRS, 94010 Créteil, France

⁴Université Paris-Saclay, CNRS, LISN, 91405, Orsay, France.

(Received 14 August 2023; revised xx; accepted xx)

We present numerical and analytical predictions of mucociliary clearance based on the continuum description of a viscoelastic mucus film, where momentum transfer from the beating cilia is represented via a Navier-slip boundary condition introduced by Bottier et al. (*PLoS Comp. Biol.*, **13**(7), 2017). Mucus viscoelasticity is represented via the Oldroyd-B model, where the relaxation time and the viscosity ratio have been fitted to experimental data for the storage and loss moduli of different types of real mucus, ranging from healthy to diseased conditions. We solve numerically the fully nonlinear governing equations for inertialess flow, and develop analytical solutions via asymptotic expansion in two limits: (i) weak viscoelasticity, i.e. low Deborah number; (ii) low cilia beat amplitude (CBA). All our approaches predict a drop in the mucus flow rate in relation to the Newtonian reference value, as the cilia beat frequency is increased. This relative drop increases with decreasing CBA and slip length. In diseased conditions, e.g. mucus properties characteristic of cystic fibrosis, the drop reaches 30% in the physiological frequency range. In the case of healthy mucus, no significant drop is observed, even at very high frequency. This contrasts with the deterioration of microorganism propulsion predicted by the low-amplitude theory of Lauga (*Phys. Fluids*, **19**(8), 2007), and is due to the larger beat amplitude and slip length associated with mucociliary clearance. In the physiological range of the cilia beat frequency, the low-amplitude prediction is accurate both for healthy and diseased conditions. Finally, we find that shear-thinning, modelled via a multi-mode Giesekus model, does not significantly alter our weakly-viscoelastic and low-amplitude predictions based on the Oldroyd-B model.

Key words:

1. Introduction

Mucociliary clearance (MCC) designates the transport of pulmonary mucus toward the trachea via the coordinated beating of cilia, which cover the epithelium within the first

† Email address for correspondence: anjishnu.choudhury@espci.fr

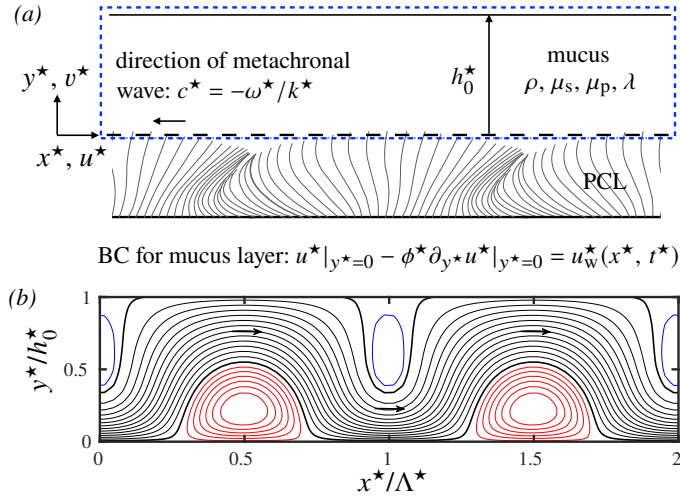


Figure 1: Continuum model of mucociliary clearance. (a) Schematic situating our model of the mucus layer (dashed blue frame) within the mucus/PCL bilayer system. Momentum transfer from the beating cilia is represented via a Navier condition (2.4b) applied at $y^*=0$ (Bottier *et al.* 2017a), introducing the wave function: $u_w^* = a^* \omega^* \cos(\theta) + \zeta \frac{1}{2} (a^*)^2 \omega^* k^* [1 - \cos(2\theta)]$, with $k^* = 2\pi/\Lambda^*$, $\theta = kx + \omega t$, and $\omega = 2\pi f$; (b) flow structure within the mucus layer for viscoelastic mucus. DNS with the code Basilisk, using the Oldroyd-B model (2.2) and periodic boundary conditions: $\lambda = 52$ ms, $\beta = 0.1$, $h_0^* = 10$ μm , $\Lambda^* = 20$ μm , $a^* = 1.6$ μm , $\phi^* = 0$, $f^* = 10$ Hz, $t^* \omega^* = 9\pi$. Streamlines in the laboratory reference frame.

33 16 airway generations of the human respiratory network. The cilia are organized in a dense
 34 brush-like array (Button *et al.* 2012) and immersed in a layer of low-viscosity Newtonian
 35 liquid, called the periciliary liquid (PCL), as shown in figure 1a. On top of the PCL layer
 36 lies a layer of viscoelastic mucus, which is responsible for capturing and evacuating alien
 37 particles and pathogens (Grotberg 2021). The non-symmetric beat cycle of individual cilia,
 38 composed of an active forward and a passive backward stroke, propagates in the form of a
 39 so-called antiplectic metachronal wave (Mitran 2007) with frequency f^* , wavelength Λ^* ,
 40 and wave speed c^* (star superscripts designate dimensional variables throughout), which
 41 imparts momentum to the mucus layer and produces a net flow in the opposite direction
 42 (Bottier *et al.* 2017a). In the present manuscript, we study the effect of viscoelasticity on this
 43 net MCC flow, both under healthy conditions and in the case of pulmonary diseases that are
 44 known to exacerbate mucus viscoelasticity (Fahy & Dickey 2010), e.g. cystic fibrosis (CF),
 45 chronic obstructive pulmonary disorder (COPD), and bronchiectasis. According to Spagnolie
 46 (2015), the reason for reduced MCC in such diseases is an open question and there is a need
 47 for predictive models that evaluate clearance efficiency versus viscoelastic characterization.
 48 Relatively few studies have accounted for the viscoelastic nature of mucus (Vanaki *et al.*
 49 2020; Sedaghat *et al.* 2023), which is imparted by mucins produced by goblet cells situated
 50 in the epithelium (Levy *et al.* 2014).

51 Smith *et al.* (2007) developed a three-layer model, where a thin *traction layer* was
 52 introduced between the PCL and mucus to account for the protrusion of cilia tips into
 53 the mucus layer (Fulford & Blake 1986). Mucus viscoelasticity was modelled via the linear
 54 Maxwell model, introducing the relaxation time λ . The authors reported a significant and
 55 non-monotonic variation of the net mucus flow rate with increasing λ . Owing to the use of
 56 the linear Maxwell model, the observed viscoelastic effect stems entirely from the traction
 57 layer. As we will show, viscoelastic corrections in the force-free mucus layer can enter the

58 problem only at $O(\text{De}^2)$, where De denotes the Deborah number $\text{De}=\lambda\omega^*$, based on the
 59 angular frequency $\omega^*=2\pi f^*$. We go beyond this limitation by accounting for non-linearity
 60 in the constitutive model, allowing us to uncover the role of viscoelasticity within the mucus
 61 layer itself, where an intricate flow pattern of counter-rotating vortices develops (figure 1b).

62 [Sedaghat et al. \(2016\)](#) used the immersed boundary method (IBM) to simulate arrays
 63 of cilia beating within a layer of airway surface liquid (representing mucus and PCL).
 64 Viscoelasticity was described with the Oldroyd-B model, introducing the viscosity ratio
 65 $\beta=\mu_s/(\mu_s + \mu_p)$, where μ_s and μ_p denote the solvent and polymer viscosities. However, the
 66 authors used a cilia density of 0.1 cilia per μm^2 which is significantly lower than typical
 67 physiological values, i.e. 5-8 cilia per μm^2 ([Bottier et al. 2017a](#)). It was not clear from this
 68 study whether viscoelasticity helps or hinders MCC in real mucus.

69 In the current study, we analyze MCC via an inertialess continuum hydrodynamic model
 70 sketched in figure 1a. We focus only on the mucus layer of height h_0^* , and model momentum
 71 transfer from the beating cilia via an experimentally-validated moving-carpet Navier-slip
 72 boundary condition (BC) applied at $y=0$ ([Bottier et al. 2017a,b](#)). This BC introduces a
 73 tangential wall velocity $u_w(x, t)$ that mimicks the metachronal wave. Mucus viscoelasticity
 74 is described with the Oldroyd-B model. Following [Vasquez et al. \(2016\)](#), we fit the model
 75 parameters, λ and β , to experimental mucus data for the storage and loss moduli G' and G''
 76 ([Hill et al. 2014](#)).

77 We solve our continuum model via two approaches. Firstly, we perform direct numerical
 78 simulations (DNS) based on the full governing equations via the finite-volume solver
 79 [Basilisk \(Popinet & collaborators 2013–2020\)](#). Secondly, we derive analytical solutions
 80 for the stream function within the mucus film, based on asymptotic expansion in two different
 81 limits: (1) the weakly-viscoelastic limit ($\text{De}\ll 1$), and (2) the limit of small cilia beat amplitude
 82 ($a\ll 1$). The low-amplitude expansion is inspired by [Lauga \(2007\)](#), who used this approach to
 83 investigate the effect of mucus viscoelasticity on the propulsion of microorganisms modelled
 84 as swimming sheets. As discussed in [Lauga \(2020\)](#), that problem is in some ways equivalent
 85 to the mucociliary transport problem considered here. However, there is one important
 86 difference. The discrete nature of the cilia, which are packed with some finite density,
 87 implies the existence of slip between the mucus and the imaginary envelope of the cilia tips.
 88 This effect is accounted for in the moving-carpet Navier BC used in the current manuscript,
 89 where we have set the slip length ϕ based on an empirical relation ([Bottier et al. 2017b](#)),
 90 linking ϕ to the cilia density. Accounting for slip represents an extension of the low-amplitude
 91 analytical solution of [Lauga \(2007\)](#), and we find that this effect is significant in the case of
 92 MCC. In contrast to the work of [Man & Lauga \(2015\)](#), who investigated the effect of wall
 93 slip on the propulsion of sheet-like microorganisms swimming in a Newtonian fluid, slip
 94 affects our problem only in the presence of viscoelasticity. This is because of the stress-free
 95 boundary condition imposed at the free surface, which implies zero average shear within the
 96 mucus layer in the Newtonian limit.

97 In terms of physical insights, we find that mucus elasticity significantly reduces MCC
 98 relative to the Newtonian limit, causing a drop in mucus flow rate that increases with
 99 increasing De , decreasing a , and decreasing slip-length ϕ . In the case of diseased mucus
 100 (characteristic of cystic fibrosis), we find a 30% reduction of MCC in the physiological
 101 frequency range, $f^*\sim 10$ Hz. By contrast, [Vasquez et al. \(2016\)](#), who also applied a continuum
 102 approach but assumed a spatially-invariant (temporally-asymmetric) wall velocity $u_w(t)$,
 103 concluded that the mucus flow rate is insensitive to mucus rheology. It turns out that our
 104 account of the metachronal cilia wave via $u_w(x, t)$ is necessary for capturing the effect of
 105 viscoelasticity on MCC. Interestingly, a flow rate reduction also occurs in the limit of a zero-
 106 mean wall velocity $\bar{u}_w=\int_0^\Lambda u_w dx=\int_0^{1/f} u_w dt=0$. In that case, viscoelasticity produces a net

negative flow rate, i.e. in the direction of the metachronal wave, as a result of memory effects. This result contrasts with Stokes' second problem for viscoelastic liquids (Mitran *et al.* 2008; Ortín 2020), where $u_w = u_w(t)$ is spatially invariant and the net flow rate is zero, and it further underlines the importance of the metachronal wave in MCC. Past studies have shown that a change in the waveform underlying the swimming motion of sheet-like microorganisms (Riley & Lauga 2015) or the geometry of the swimmer itself (Angeles *et al.* 2021) can switch the effect of viscoelasticity from hindering to enhancing propulsion.

Although we mainly focus on the role of viscoelasticity by using the Oldroyd-B model, we have also checked the additional effect of shear-thinning, another known non-Newtonian property of mucus (Jory *et al.* 2022). For this, we have employed the Giesekus model, which accurately accounts for both viscoelasticity and shear-thinning properties of mucus (Vasquez *et al.* 2016; Sedaghat *et al.* 2022). We find that neither our low-amplitude nor our weakly-viscoelastic predictions are significantly affected by shear-thinning. This is due to the nature of the associated nonlinear terms in the Giesekus model, which are quadratic in the stresses and scaled by the Deborah number. As a result, shear-thinning is weak at small amplitudes and subordinate to viscoelasticity. We find that this leads to a qualitatively different MCC response versus a generalized Newtonian description of mucus via the Carreau model (Chatelin *et al.* 2017).

Our manuscript is structured as follows. In section 2, we introduce the governing equations constituting our mathematical model of MCC. Next, in section 3, we quantify the viscoelastic properties of the different types of mucus considered in our computations, as well as relevant kinematic parameters linked to MCC. Section 4 details the methods employed. In subsection 4.1, we derive analytical solutions for the mucus flow rate based on asymptotic expansion in different limits. In subsection 4.2, we describe the solver employed for our DNS. Results are presented in section 5, where we first focus on characterizing the effect of viscoelasticity on the mucus flow rate (subsection 5.1) by comparing with the Newtonian limit. Then, in subsection 5.2, we discuss the additional effect of shear-thinning via calculations based on the (multi-mode) Giesekus model. Conclusions are drawn in section 6, and the manuscript is completed by appendices A and B, where we have written out several expressions intervening in the analytical solutions derived in subsection 4.1.

2. Mathematical description

We consider a viscoelastic mucus layer of constant height h_0^* on the interval $y^*=0$ to $y^*=h_0^*$, as sketched in Figure 1a. The mucus rheology is represented via the Oldroyd-B model, with solvent and polymeric viscosities μ_s and μ_p , and relaxation time λ . Both the Reynolds number $Re = \rho h_0^{*2} \omega^* / \mu_s \sim 10^{-3}$ and the capillary number $Ca = \mu_s h_0^* \omega^* / \sigma \sim 10^{-3}$, where ρ and σ denote the liquid mass density and surface tension, are small and thus we assume inertialess flow and a flat surface of the mucus layer (Smith *et al.* 2007). In this limit, the flow is governed by the (dimensionless) continuity and Stokes equations with additional polymeric viscous stresses τ_{ij} :

$$\partial_x u + \partial_y v = 0, \quad (2.1a)$$

$$0 = -\partial_x p + (\partial_{xx} u + \partial_{yy} u) + \partial_x \tau_{xx} + \partial_y \tau_{xy}, \quad (2.1b)$$

$$0 = -\partial_y p + (\partial_{xx} v + \partial_{yy} v) + \partial_x \tau_{xy} + \partial_y \tau_{yy}, \quad (2.1c)$$

where we have scaled lengths with $\mathcal{L} = h_0^*$, velocities with $\mathcal{U} = h_0^* \omega^*$, and τ_{ij} as well as pressure p with $\mathcal{P} = \mu_s \mathcal{U} / \mathcal{L}$, using the angular frequency of the cilia beat cycle ω^* . The components of the polymeric stress tensor τ_{ij} are governed by the upper-convected Maxwell

152 (UCM) model:

$$153 \quad \tau_{xx} + \text{De} \left[\partial_t \tau_{xx} + u \partial_x \tau_{xx} + v \partial_y \tau_{xx} - 2\tau_{xx} \partial_x u - 2\tau_{xy} \partial_y u \right] = 2 \frac{1-\beta}{\beta} \partial_x u, \quad (2.2a)$$

$$154 \quad \tau_{xy} + \text{De} \left[\partial_t \tau_{xy} + u \partial_x \tau_{xy} + v \partial_y \tau_{xy} - \tau_{xx} \partial_x v - \tau_{yy} \partial_y u \right] = \frac{1-\beta}{\beta} (\partial_y u + \partial_x v), \quad (2.2b)$$

$$155 \quad \tau_{yy} + \text{De} \left[\partial_t \tau_{yy} + u \partial_x \tau_{yy} + v \partial_y \tau_{yy} - 2\tau_{xy} \partial_x v - 2\tau_{yy} \partial_y v \right] = 2 \frac{1-\beta}{\beta} \partial_y v, \quad (2.2c)$$

157 where we have scaled time with $\mathcal{T}=1/\omega^*$, yielding the Deborah number $\text{De} = \lambda\omega^*$, and the
 158 viscosity ratio $\beta = \mu_s / (\mu_s + \mu_p)$. The system is closed with the following boundary conditions.
 159 At the film surface, $y=1$, we impose:

$$160 \quad \partial_y u + \tau_{xy} = 0, \quad (2.3a)$$

$$161 \quad v = 0, \quad (2.3b)$$

163 where we have assumed impermeability and neglected viscous stresses in the gas above the
 164 mucus layer. At the bottom boundary, $y=0$, we impose the Navier-slip boundary condition
 165 introduced by [Bottier et al. \(2017b\)](#) for modelling momentum transfer from the beating cilia:
 166

$$167 \quad u - \phi \partial_y u = u_w(x, t), \quad v = 0, \quad (2.4a)$$

168 where ϕ denotes the (dimensionless) slip length. Here, the cilia kinematics is represented via
 169 the wave function $u_w(x, t)$:

$$170 \quad u_w(x, t) = a \cos(kx + t) + \zeta \frac{1}{2} a^2 k [1 - \cos\{2(kx + t)\}], \quad (2.4b)$$

171 introducing the cilia beat amplitude a , and the metachronal wave number $k=2\pi/\Lambda$, where
 172 the dimensionless wavelength $\Lambda = \Lambda^*/h_0^*$, due to the scaling chosen, sets the aspect ratio of
 173 our geometry. Without loss of generality, we have phase shifted $u_w(x, t)$ by $\pi/2$ w.r.t. the
 174 classical formulation of [Bottier et al. \(2017b\)](#). The parameter ζ is a binary parameter that
 175 takes values $\zeta=0$ and $\zeta=1$, and can be used to deactivate the second and third RHS terms in
 176 (2.4b). In that limit, i.e. $\zeta=0$, the phase average \bar{u}_w is zero, which, in the case of a Newtonian
 177 fluid, leads to a symmetrical cellular flow pattern (e.g. figure 2a). This reference case is
 178 convenient for illustrating the signature of viscoelasticity, which tends to break the symmetry
 179 of the flow field (e.g. figure 6e). The *moving carpet* boundary condition written in (2.4) has
 180 been validated versus particle image velocimetry (PIV) measurements in the vicinity of live
 181 beating cilia ([Bottier et al. 2017a](#)).

182 As a key observable in our study, we evaluate the net mucus flow rate q :

$$183 \quad q = \int_0^1 u \, dy, \quad (2.5)$$

184 which is spatially invariant due to continuity and the flat-surface assumption, i.e. $\partial_x q = -\partial_t h = 0$,
 185 and time invariant due to the wave-nature of u_w (2.4b). In the Newtonian limit (subscript
 186 N), the governing equations become linear, and, thus, the flow field is a simple superposition
 187 of the solutions associated with the three terms in the wave function (2.4b). Because the
 188 phase-average of the two harmonic terms is zero, only the constant term contributes to the
 189 net flow, yielding:

$$190 \quad q_N = \zeta q_{\text{ref}}, \quad \text{with} \quad q_{\text{ref}} \equiv \frac{1}{2} a^2 k, \quad (2.6)$$

Mucus type	G' (Pa)	G'' (Pa)	λ (ms)	β	a^* (μm)
HBE-2 wt%	0.02	0.179	3	0.4	5
HBE-3 wt%	0.12	0.3	10	0.19	4
HBE-4 wt%	0.3	0.5	16	0.13	3
HBE-5 wt%	9.09	2.98	52	0.002	1.6

Table 1: Human bronchial epithelium (HBE) mucus types and cilia beat amplitude a^* used in our simulations. Measurement data for G' and G'' , ranging from healthy to diseased mucus, are taken at $f^* \sim 10$ Hz from Hill *et al.* (2014). Oldroyd-B model parameters λ and β were fitted via (3.1), assuming $\mu_s = 1$ mPa-s.

191 which corresponds to a plug flow with wall velocity $u_w = \zeta a^2 k / 2$. Throughout the paper, we
192 will use q_N (and q_{ref}) as a reference value to quantify the effect of viscoelasticity.

193 3. MCC scenarios: mucus types and cilia parameters

194 Experimentally, the mechanical response of viscoelastic mucus is quantified via the complex
195 modulus $G = G' + iG''$, containing the storage and loss moduli G' and G'' , which are related
196 to the parameters of the Oldroyd-B model according to Siginer (2014):

$$197 \quad \frac{G'}{\mu_s \omega^*} = \frac{(1 - \beta)}{\beta} \frac{\lambda \omega^*}{1 + (\lambda \omega^*)^2}, \quad \frac{G''}{\mu_s \omega^*} = 1 + \frac{(1 - \beta)}{\beta [1 + (\lambda \omega^*)^2]}. \quad (3.1)$$

199 We focus on four types of mucus corresponding to Human Bronchial Epithelial (HBE)
200 cultures with varying mucin concentration (Hill *et al.* 2014), ranging from healthy patients
201 (2 wt%) to patients diagnosed with CF or COPD (5 wt%). The properties of these mucus
202 types are provided in table 1. We have assumed water as the solvent phase, i.e. $\mu_s = 1$ mPa-s,
203 and fitted β and λ to experimental values of G' and G'' (Hill *et al.* 2014) at a representative
204 cilia beat frequency $f^* \sim 10$ Hz. Accounting for the frequency dependence of β and λ does
205 not change our results significantly (as will be shown in figure 3a).

206 In the case of CF, the PCL layer is depleted in favor of the mucus layer, which can
207 considerably reduce the mucus velocity imparted by the cilia (Guo & Kanso 2017). We
208 account for this by adjusting the beat amplitude a in terms of the mucin concentration
209 (see table 1), by interpolating between experiments for healthy mucus (Bottier *et al.* 2017a),
210 $a^* = 5 \mu\text{m}$, and diseased mucus (Bottier *et al.* 2022), $a^* = 1.6 \mu\text{m}$.

211 Bottier *et al.* (2017a) established experimentally a relation between the cilia density and
212 the slip length ϕ^* . We use a cilia density of 86% in our simulations, which is representative
213 of the patient data reported in that reference, yielding a slip length of $\phi^* = 10 \mu\text{m}$.

214 4. Methods

215 4.1. Analytical solutions via asymptotic expansion

216 We obtain analytical solutions for our boundary value problem (2.1)-(2.4) in two different
217 limits: (i) small Deborah number ($\text{De} \ll 1$), and (ii) small cilia beat amplitude ($a \ll 1$). For
218 this, we introduce the stream function Ψ :

$$219 \quad \partial_y \Psi = u, \quad -\partial_x \Psi = v, \quad (4.1)$$

220 to which we apply a regular perturbation expansion:

$$221 \quad \Psi(x, y, t) = \Psi_0(x, y, t) + \epsilon \Psi_1(x, y, t) + \epsilon^2 \Psi_2(x, y, t), \quad (4.2)$$

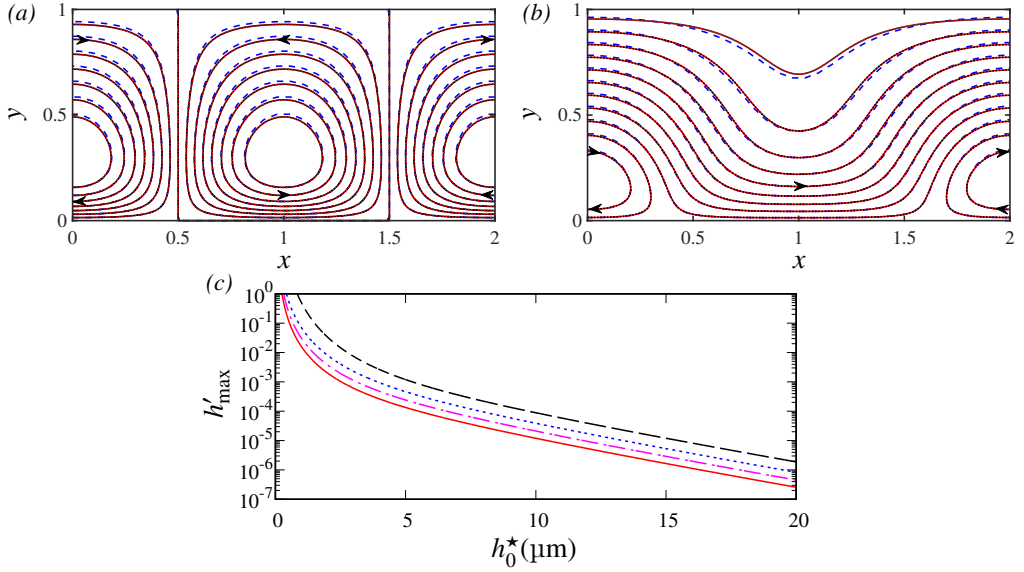


Figure 2: Flow structure within the mucus film. Newtonian limit: $De=0$, $\Lambda^*=20 \mu\text{m}$. (a,b) Streamlines for two forms of the wave function (2.4b): $a^*=1.6 \mu\text{m}$, $\phi^*=0$, $t=\pi$. Solid red: analytical solution (4.3a), dashed blue: DNS using $\Delta x=1/64$, dotted black (almost perfectly overlapping solid red): DNS using $\Delta x=1/128$. (a) $\zeta=0$: cellular flow pattern; (b) $\zeta=1$: meandering flow; (c) estimation of maximum film surface deflection according to (4.5) for different values of the slip length ϕ^* : $a^*=5 \mu\text{m}$, $Ca=1 \times 10^{-3}$. Dashed: $\phi^*=0$, dotted: $\phi^*=2 \mu\text{m}$, dot-dashed: $\phi^*=5 \mu\text{m}$, solid: $\phi^*=10 \mu\text{m}$.

222 where the small parameter ϵ is either De or a , depending on the expansion considered. Then,
 223 introducing (4.2) into (2.1)-(2.4) and truncating appropriately, we may obtain Ψ_i order by
 224 order. We point out that Ψ_0 is the solution of the biharmonic equation, obtained by eliminating
 225 pressure from the truncated forms of (2.1b) and (2.1c) via cross differentiation.

226 In the weakly-viscoelastic limit, we expand in terms of $\epsilon=De$ and obtain at $O(De^2)$:

$$227 \quad \Psi_0(x, y, t) = \left[(A_1 + B_1 ky)e^{ky} + (C_1 + D_1 ky)e^{-ky} \right] \cos(kx + t) + \zeta A_2 y$$

$$228 \quad + \zeta \left[(A_3 + 2B_3 ky)e^{2ky} + (C_3 + 2D_3 ky)e^{-2ky} \right] \cos\{2(kx + t)\}, \quad (4.3a)$$

$$229 \quad \Psi_1(x, y, t) = 0, \quad (4.3b)$$

$$230 \quad \Psi_2(x, y, t) = \Psi_H(x, y, t) + \Psi_P(x, y, t), \quad (4.3c)$$

231 where A_i , B_i , C_i , and D_i are integration constants, and $\Psi_H(x, y, t)$ and $\Psi_P(x, y, t)$ denote
 232 homogenous and particular solutions, which are all written out in appendix A, and in a
 233 supplementary Mathematica notebook. A simple relation for the flow rate $q = \Psi|_{y=1} - \Psi|_{y=0}$
 234 can be obtained by considering (4.3) in the limit $\zeta=0$:

$$235 \quad \left. \frac{q}{q_{\text{ref}}} \right|_{\zeta=0} = -(1 - \beta)De^2 \frac{(S^2 + 6k\phi SC)}{(S + 2k\phi C)^2} + O(De^3), \quad (4.4)$$

236 where $S = \sinh(2k) - 2k$ and $C = \cosh(2k) - 1$. We see that viscoelasticity enters at $O(De^2)$, and
 237 constitutes a negative flow rate contribution. The full form of q/q_{ref} for $\zeta=1$ is too long to
 238 be written here. Instead, we provide it in the supplementary Mathematica notebook. In the
 239 Newtonian limit ($De=0$), (4.2) reduces to Ψ_0 , which we have plotted in figures 2a and 2b for

240 the reduced ($\zeta=0$) and full ($\zeta=1$) form of (2.4b), respectively. In the former case, the flow
241 pattern is cellular (figure 2a), and, in the latter, it is meandering (figure 2b).

242 The leading-order solution Ψ_0 can also be used to estimate the deflection of the liquid-gas
244 interface h' :

$$245 \quad h' = \text{Ca} \left\{ \frac{4a \cosh(k)}{S + 2k\phi C} - \frac{4a^2 k \zeta \cosh(2k) \cos(kx + t)}{S' + 2k'\phi C'} \right\} \sin(kx + t), \quad (4.5)$$

246 where $S' = \sinh(2k') - 2k'$ and $C' = \cosh(2k') - 1$, introducing $k' = 2k$. This relation is obtained
247 by balancing the normal stress acting at our flat liquid-gas interface, $y=1$, with the capillary
248 pressure jump of a deformable film surface, $h=1+h'$:

$$249 \quad p - 2\partial_y v - \tau_{yy} = -\text{Ca}^{-1} \partial_{xx} h, \quad (4.6)$$

250 where we have neglected the gas stresses, then truncating at $O(\text{De}^0)$, and substituting the
251 leading-order solutions for Ψ (4.3a) and for p (4.7) into (4.6). The leading-order pressure,
252 p_0 , is obtained by integrating (2.1c) in y -direction and (2.1b) in x -direction, after having
254 applied (4.2), truncated, and substituted (4.3a):

$$255 \quad p_0 = 2e^{-2ky} k^2 \sin(kx + t) \{ e^{ky} (D_1 + B_1 e^{2ky}) + 8\zeta \cos(kx + t) (D_3 + B_3 e^{4ky}) \}, \quad (4.7)$$

256 where, without loss of generality, we have assumed $p_0(x=0, y=0, t)=0$.

257 Figure 2c represents the maximum displacement h'_{\max} obtained from (4.5) versus the
258 dimensional film height h_0^* , demonstrating that our flat-surface assumption ($\partial_x h = \partial_{xx} h = 0$)
259 is valid within the physiological film thickness range $h_0^* = 5\text{--}20 \mu\text{m}$, for the largest cilia beat
260 amplitude considered, i.e. $a^* = 5 \mu\text{m}$.

261 In the low-amplitude limit, we expand (4.2) in terms of $\epsilon = a$ and seek a solution for the
262 time-averaged stream function $\bar{\Psi}(y)$. For $\zeta=1$, we obtain:

$$263 \quad \bar{\Psi}(y) = a^2 \bar{\Psi}_2(y) + O(a^3), \quad (4.8)$$

$$264 \quad \bar{\Psi}_2(y) = \left(I_0 + I_1 y + I_2 y^2 \right) e^{2ky} + \left(J_0 + J_1 y + J_2 y^2 \right) e^{-2ky} + K_1 y + K_2 y^2,$$

265 where the constants I_i , J_i , and K_i are given in appendix B. Based on (4.8), we obtain the
266 normalized flow rate:

$$267 \quad \frac{q}{q_N} = 1 - \frac{(1 - \beta) \text{De}^2 (S^2 + 6\phi k S C)}{(1 + \text{De}^2)(S + 2\phi k C)^2} + O(a^3). \quad (4.9)$$

268 In the no-slip limit $\phi=0$, (4.9) collapses with equation (26) in Lauga (2007), which predicts
269 the normalized swimming speed U/U_N of microorganisms represented as Taylor swimming
270 sheets. In figure 3a, we have plotted the average mucus velocity $\bar{u}^* = q^*/h_0^*$ based on (4.9)
271 versus the cilia beat frequency f^* . The dot-dashed and dashed red curves correspond to
272 viscoelastic mucus, assuming constant (dot-dashed) or frequency-dependent (dashed) values
273 of G' and G'' , based on experimental data of Hill *et al.* (2014). Comparing these curves,
274 we may conclude that our approximation to neglect the frequency-dependence of G' and
275 G'' is reasonable in the considered frequency range. The solid black curve in figure 3a
276 corresponds to the Newtonian limit ($\text{De}=0$), where q^* increases linearly with f^* (Blake
277 1973; Sedaghat *et al.* 2016). The exact relation underlying this curve is $q^* = q_N^* = \pi a^{*2} k f^*$,
278 which follows from (2.6) upon re-dimensionalizing with the scale $\mathcal{UL} = h_0^{*2} \omega^*$.

279

4.2. Direct numerical simulation

280 We solve numerically the fully nonlinear governing equations (2.1)-(2.4) on a periodic
281 domain using the academic code Basilisk, which employs the log-conform approach

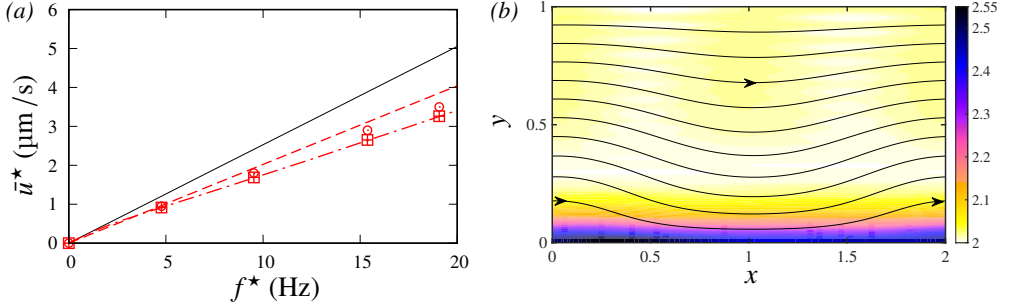


Figure 3: Features of the flow within a viscoelastic mucus layer: HBE-5wt% mucus, $h_0^* = 10 \mu\text{m}$, $\Lambda^* = 20 \mu\text{m}$, $a^* = 1.6 \mu\text{m}$, $\phi^* = 10 \mu\text{m}$. (a) Average mucus velocity $\bar{u}^* = q^*/h_0^*$. Solid: Newtonian limit, dot-dashed: based on (4.9) with $\lambda = 52 \text{ ms}$, $\beta = 0.1$, dashed: based on (4.9) with frequency dependent λ and β according to G' and G'' data in Hill *et al.* (2014), symbols: our DNS. Circles: $\Delta x = 1/32$, squares: $\Delta x = 1/64$, plus signs: $\Delta x = 1/128$; (b) streamlines and contours of the trace $\text{tr}(\mathbf{C})$ of the conformation tensor $\mathbf{C} = \text{De} \tau_{ij} + \mathbf{I}$ based on the Oldroyd-B model: $\lambda = 52 \text{ ms}$, $\beta = 0.1$, $f^* = 19 \text{ Hz}$, $t = 9\pi$.

282 (López-Herrera *et al.* 2019) for resolving the constitutive relations (2.2). It is a pressure-
 283 based solver, and thus the Poisson equation for the pressure is solved instead of (2.1a) to
 284 enforce continuity (Popinet 2015), using the boundary conditions $\partial_y p = 0$ at $y = 0$ and (4.6) at
 285 $y = h$, in the limit $h = 1$. The same code was recently used by Romano *et al.* (2021) to investigate
 286 the effect of viscoelasticity on airway occlusion, and validated versus several relevant
 287 benchmarks. The code relies on a finite-volume spatial discretization, using the second-
 288 order upwind Bell–Collela–Glaz advection scheme (Bell *et al.* 1989). Time discretization is
 289 implicit for diffusion and explicit for advection terms, and the time step is adapted according
 290 to a CFL criterion. Our DNS were typically performed on a uniform quadtree grid, with grid
 291 size $\Delta x = 2^{-6} = 1/64$, and the time step was limited by a lower bound $\Delta t = 10^{-7}$. A typical DNS
 292 run took 5-18 hours on 8 CPUs to reach a fully developed state (after 3-10 periods).

293 In figures 2a and 2b, we have included grid convergence results obtained with our DNS
 294 for the Newtonian reference case. Dashed blue curves correspond to a grid size of $\Delta x = 1/64$,
 295 and dotted black curves to $\Delta x = 1/128$. Agreement with our analytical predictions (solid red
 296 curves) according to (4.3a) is visually perfect for the fine grid and remains excellent for
 297 the reference grid. The same conclusion can be drawn from figure 3a, which confronts DNS
 298 using three different grids (symbols) with our low-amplitude asymptotic solution (dot-dashed
 299 curve) according to (4.9), for a viscoelastic mucus film.

300 Figure 3b represents streamlines for one of our DNS from figure 3a. In the same plot,
 301 we have represented contours of the trace $\text{tr}(\mathbf{C})$ of the conformation tensor $\mathbf{C} = \text{De} \tau_{ij} + \mathbf{I}$
 302 based on the Oldroyd-B model, where \mathbf{I} is the identity matrix. The quantity $\text{tr}(\mathbf{C})$ allows to
 303 gauge the polymer extension associated with our flow field. We find that the maximum value,
 304 observed near the cilia-mucus interface, is $\text{tr}(\mathbf{C}) \sim 2.5$, which implies a moderate fluid element
 305 extension relative to the Newtonian limit $\text{tr}(\mathbf{C}) = 2$. Thus, the Oldroyd-B model employed here
 306 is expected to behave well for our flow.

307 In our problem, the mucus viscosities μ_s and μ_p intervene only via β . Thus, the total
 308 viscosity $\mu = \mu_s + \mu_p$ can be chosen freely. For numerical convenience, we choose a low value
 309 $\mu = 1 \text{ mPa}\cdot\text{s}$, allowing us to limit the viscous-diffusion time scale. The log-conform approach
 310 is an effective remedy against numerical instabilities associated with large values of De
 311 (Fattal & Kupferman 2005), and we have encountered no such instabilities in our DNS.
 312 However, in our simulations of HBE-5wt% mucus, we needed to increase β from its target
 313 value $\beta = 0.002$ to $\beta = 0.1$, because of the degeneracy of the constitutive relations (2.2) in the

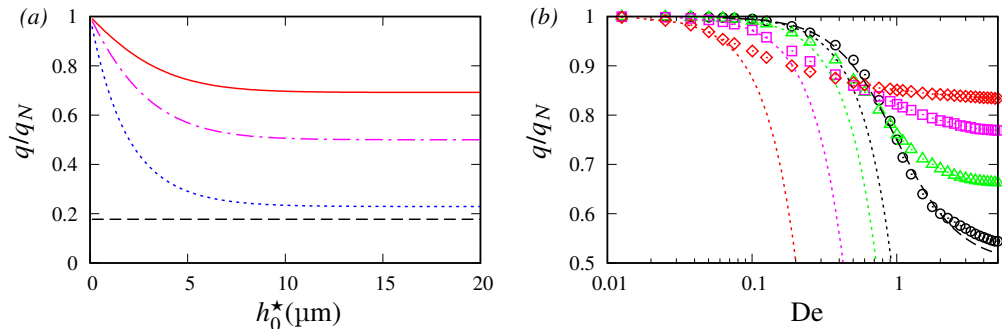


Figure 4: Effect of slip length ϕ and CBA a on the MCC flow rate of viscoelastic mucus: $\Lambda^*=20\ \mu\text{m}$. (a) Effect of slip-length: $\text{De}=3$, $\beta=0.1$. Low-amplitude prediction (4.9). Dashed: $\phi^*=0$, dotted: $\phi^*=2\ \mu\text{m}$, dot-dashed: $\phi^*=5\ \mu\text{m}$, solid: $\phi^*=10\ \mu\text{m}$. (b) Effect of CBA: $\phi=0$, $\beta=0.5$, $h_0^*=10\ \mu\text{m}$. Dotted: based on low-De prediction (4.3), dashed line: (4.9), symbols: DNS. Circles: $a^*=1.6\ \mu\text{m}$, triangles: $a^*=3\ \mu\text{m}$, squares: $a^*=5\ \mu\text{m}$, diamonds: $a^*=8\ \mu\text{m}$.

314 limit $\beta \rightarrow 0$. We have checked via (4.9) that this change in β has no appreciable effect on the
 315 MCC flow rate.

316 5. Results and discussion

317 Our main results are presented in subsection 5.1, where we focus solely on the effect
 318 of viscoelasticity. In subsection 5.2, we will discuss the additional implications of shear-
 319 thinning, which is another non-Newtonian property of mucus.

320

5.1. Role of viscoelasticity

321 We seek to quantify the effect of mucus viscoelasticity on MCC by comparing the actual flow
 322 rate q (2.5) to its Newtonian limit q_N . For this, we characterize the ratio q/q_N versus three
 323 control parameters of our problem, i.e. De , ϕ , and a . We start with figure 4 by establishing
 324 the effect of the slip length ϕ and beat amplitude a , in order to assess to what extent the no-
 325 slip low-amplitude theory of Lauga (2007) is applicable to the MCC problem studied here.
 326 Figure 4a shows predictions of q/q_N based on our low-amplitude solution (4.9) for different
 327 slip lengths ϕ and representative values of De and β . Firstly, we see that viscoelasticity can
 328 greatly reduce the MCC flow rate ($q/q_N < 1$). Secondly, this effect is much larger in the no-slip
 329 limit (long dashes) than for realistic values of ϕ (solid curve). Thirdly, the no-slip limit cannot
 330 represent the q/q_N variation in terms of the film height h_0^* .

331 Figure 4b represents the effect of the CBA a in the no-slip limit $\phi=0$ via DNS data
 332 (symbols). We see that q/q_N becomes very small at the lowest CBA (circles, $a^*=1.6\ \mu\text{m}$),
 333 which corresponds to CF conditions. The low-amplitude analytical prediction (4.9) (black
 334 dashed curve) is able to accurately capture this scenario versus the DNS (open circles).
 335 By contrast, a significant discrepancy is observed for the CBA corresponding to healthy
 336 conditions (diamonds, $a^*=8\ \mu\text{m}$). Thus, the low-amplitude asymptotic expansion is not
 337 applicable in the entire physiological range of MCC, owing to potentially large values of
 338 CBA. The dotted curves in figure 4b represent our low-De solution (4.3). These show good
 339 agreement with the DNS for low values of De , but cannot predict the levelling off of q/q_N
 340 with increasing De . The deviation from the DNS data sets in at lower values of De the larger
 341 a becomes.

342 We now turn to the MCC scenarios characterized in table 1. If not otherwise mentioned, we
 343 use $h_0^*=10\ \mu\text{m}$, $\phi^*=10\ \mu\text{m}$, and $\Lambda^*=20\ \mu\text{m}$. Figures 5a and 5b represent DNS and analytical

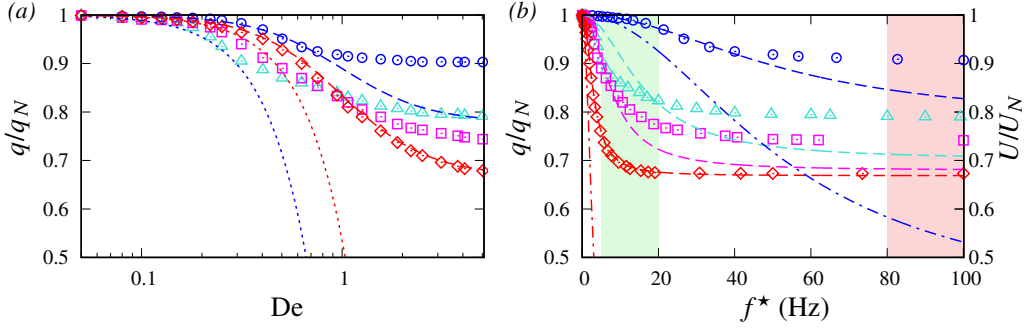


Figure 5: Viscoelasticity-induced flow rate reduction for mucus types from table 1: $\phi^* = 10 \mu\text{m}$, $h_0^* = 10 \mu\text{m}$, $\Lambda^* = 20 \mu\text{m}$. Symbols: DNS. Blue circles: HBE-2wt%, cyan triangles: HBE-3wt%, magenta squares: HBE-4wt%, red diamonds: HBE-5wt%, dotted lines: (4.3), dashed lines: (4.9). (a) Versus Deborah number $De = \lambda\omega^*$; (b) versus cilia beat frequency f^* . Dot-dashed lines (right ordinate): normalized swimming speed U/U_N of microorganisms according to Lauga (2007). Green/pink shaded regions mark frequency range for MCC and microorganism propulsion, respectively.

344 predictions of q/q_N for the four considered mucus types versus the Deborah number De and
 345 versus the cilia beat frequency f^* , respectively. In the case of healthy mucus (HBE-2 wt%,
 346 blue circles), which is characterized by a rather small relaxation time λ , viscoelasticity reduces
 347 MCC only slightly ($q/q_N \sim 0.995 - 0.98$) within the physiological frequency range $f^* = 5$ –
 348 20 Hz (green shaded region in figure 5b). This contrasts with the very significant reduction
 349 in the swimming speed U of non-ciliated microorganisms (dot-dashed blue curve), which
 350 operate at much greater frequencies ($f^* > 80$ Hz, pink shaded region) and do not experience
 351 slip, as predicted by the theory of Lauga (2007). We point out however that particular types of
 352 swimming motions and swimmer geometries can lead to a viscoelasticity-induced increase
 353 of the swimming speed (Riley & Lauga 2015; Angeles *et al.* 2021).

354 In the case of mucus corresponding to CF conditions (HBE-5wt%, red diamonds in figure
 355 5), which displays a much greater relaxation time λ , the MCC flow rate drops by as much
 356 as 30% versus the Newtonian limit. This is mainly due to the reduced CBA associated
 357 with CF conditions. Dashed curves in figure 5b represent our low-amplitude analytical
 358 prediction (4.9). Upon comparing these with our DNS data (symbols), we may conclude
 359 that the analytical prediction accurately captures q/q_N in the MCC frequency range for the
 360 healthy mucus (circles) and for the most unhealthy mucus (diamonds). However, significant
 361 deviations are observed for the intermediate mucus types (triangles and squares).

362 Next, we turn to the mechanism underlying the viscoelasticity-induced flow rate drop
 363 observed in figure 5. To this end, it is useful to reduce the problem to a simpler version
 364 by setting $\phi = 0$ and $\zeta = 0$ in (2.4b), which leads to $\bar{u}_w = 0$. We have shown in figure 2a that
 365 the corresponding flow pattern in the Newtonian limit is cellular and symmetrical, and,
 366 consequently, $q = q_N = 0$. Adding viscoelasticity, which we now know to affect the flow rate q ,
 367 will thus cause a topological change in the flow field.

368 Figure 6a demonstrates via DNS data (symbols) that a similar flow rate reduction is
 369 observed for the reduced form of the wave function (2.4b), i.e. $\zeta = 0$ (squares), as compared to
 370 the full form, i.e. $\zeta = 1$ (circles). Further, the mucus flow rate q becomes negative for $\zeta = 0$, and
 371 this effect holds at arbitrarily low De . The effect is captured by our low- De solution (4.4),
 372 which is represented via a dotted blue curve in figure 6a. Figure 6b shows how viscoelasticity
 373 modifies the flow field in this limit, by plotting Ψ_0 and Ψ_2 according to (4.3). We see that
 374 the $O(De^2)$ correction (dashed lines) causes a net flow to the left, which distorts the $O(De^0)$
 375 cellular flow pattern (solid lines) when superimposed on the latter. Figures 6c–6f display the

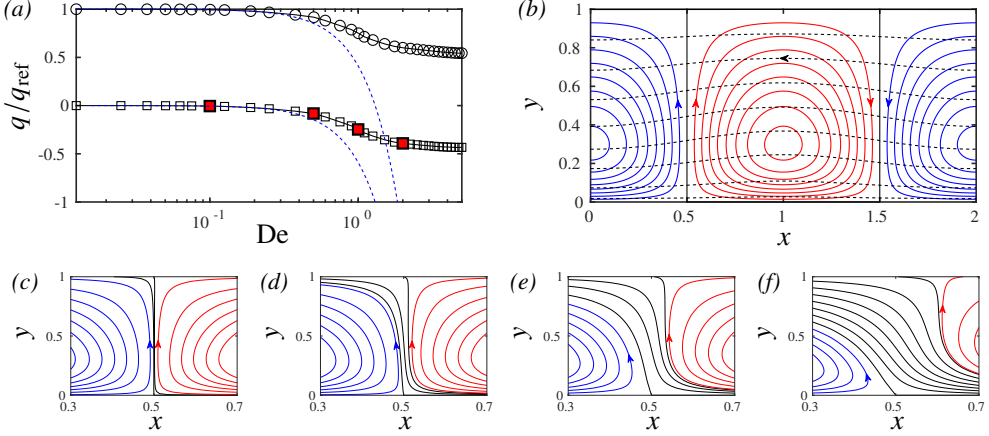


Figure 6: Change in flow topology within a viscoelastic mucus film under an increase of the cilia beat frequency: HBE-5 wt% (see table 1), $\phi=0$, $a^*=1.6 \mu\text{m}$, $\Lambda^*=20 \mu\text{m}$, $h_0^*=10 \mu\text{m}$. (a) Normalized flow rate for two forms of (2.4b). Circles: DNS for $\zeta=1$, squares: DNS for $\zeta=0$, dotted blue curves: low-De solutions based on (4.3); (b) Ψ_0 (solid) and Ψ_2 (dashed) according to (4.3): $De=0.1$; (c-f) streamlines from DNS corresponding to filled squares in panel a, showing the emergence of a negative meander (black lines) sandwiched between clockwise (red lines) and anti-clockwise (blue lines) vortices, as De is increased. (c) $De=0.1$; (d) $De=0.5$; (e) $De=1$; (f) $De=2$.

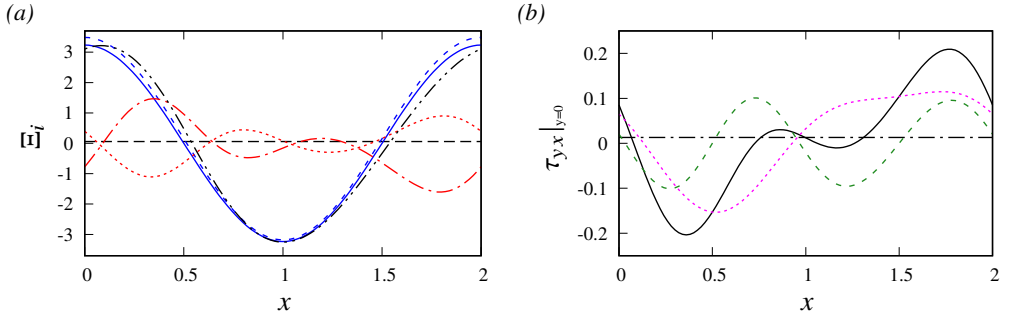


Figure 7: Mechanism underlying the negative meander in figure 6: $\phi=0$, $\zeta=0$, $h_0^*=10 \mu\text{m}$, $\Lambda^*=20 \mu\text{m}$, $De=0.1$. (a) Profiles of terms Ξ_i in the x -momentum equation (2.1b) evaluated at $y=0$, based on our low-De solution (4.3), and their phase averages $\bar{\Xi}_i$. Dashed: $\Xi_1=\partial_{xx}u+\partial_{yy}u$, $\bar{\Xi}_1=0.18$, solid: $\Xi_0=\Xi_1|_{De=0}=\partial_{xx}u^{(0)}+\partial_{yy}u^{(0)}$, $\bar{\Xi}_0=0$, dotted: $\Xi_2=\partial_x\tau_{xx}$, $\bar{\Xi}_2=0.004$, dot-dashed: $\Xi_3=\partial_y\tau_{yx}$, $\bar{\Xi}_3=-0.16$, dot-dot-dashed: $\Xi_4=\partial_x p$, $\bar{\Xi}_4=0.024$ (long dashes); (b) polymeric wall shear stress τ_{yx}^{VE} according to (5.1). Solid: τ_{yx}^{VE} , $\bar{\tau}_{yx}^{\text{VE}}=0.013$ (dot-dashed), dashed: τ_{yx}^{res} , $\bar{\tau}_{yx}^{\text{res}}=0.0003$, dotted: τ_{yx}^{mem} , $\bar{\tau}_{yx}^{\text{mem}}=0.0127$.

376 total flow field obtained from DNS for the points marked by filled symbols in figure 6a. We see
 377 that viscoelasticity causes a negative meander (as opposed to the positive meander observed
 378 in figures 1b and 2b), which winds between the counter-rotating vortices and increases in
 379 thickness as De is increased (from panels 6c to 6f). This negative meander transports mucus
 380 in the direction of the metachronal wave, i.e. in the negative x -direction, and, thus, the wrong
 381 direction from the point of view of MCC. It is associated with the $\cos(kx+t)$ term in the
 382 wall velocity u_w (2.4b), and, in the full MCC problem ($\zeta=1$), it opposes the positive flow
 383 induced by the term with the form $a^2k/2$.

384 To unravel what causes the negative meander observed in figure 6, we analyze the different
 385 terms in the x -momentum equation (2.1b) evaluated at $y=0$, based on our low-De solution

(4.3) in the limit $\zeta=\phi=0$. Profiles of these terms, which we denote Ξ_i , are plotted in figure 7a, and their phase averages $\bar{\Xi}_i$ are given in the caption. The dashed blue curve represents the contribution of the solvent stresses $\Xi_1=\partial_{xx}u+\partial_{yy}u$, which allows to gauge the degree of symmetry of the flow field. This curve is shifted toward positive values compared to the Newtonian limit $\Xi_0=\Xi_1|_{De=0}=\partial_{xx}u^{(0)}+\partial_{yy}u^{(0)}$ (solid blue curve, $\bar{\Xi}_0=0$), i.e. its phase average is non-zero ($\bar{\Xi}_1=0.18$), indicating a viscoelasticity-induced loss of symmetry. This is mainly caused by the contribution of the tangential polymeric stress $\Xi_3=\partial_y\tau_{yx}$ (dot-dashed red curve, $\bar{\Xi}_3=-0.16$), the contributions of the normal stress $\Xi_2=\partial_y\tau_{yx}$ (dotted red curve, $\bar{\Xi}_3=0.004$) and the pressure $\Xi_2=\partial_x p$ (dot-dot-dashed black curve, $\bar{\Xi}_2=0.024$) being weaker.

We focus next on the tangential polymeric stress at $y=0$:

$$\tau_{yx}|_{y=0} = \frac{1-\beta}{\beta} \partial_y u^{(0)}|_{y=0} + \underbrace{\text{De} \tau_{yx}^{(1)}|_{y=0} + \text{De}^2 \tau_{yx}^{(2)}|_{y=0}}_{\tau_{yx}^{\text{VE}}} + O(\text{De}^3), \quad (5.1a)$$

where τ_{yx}^{VE} is the viscoelastic contribution, which we decompose formally into a memory term τ_{yx}^{mem} , containing all time derivatives intervening through (2.2), and a residual term τ_{yx}^{res} , containing all other contributions:

$$\tau_{yx}^{\text{VE}} \equiv \tau_{yx}^{\text{mem}} + \tau_{yx}^{\text{res}}. \quad (5.1b)$$

Figure 7b represents profiles of τ_{yx}^{VE} (solid black), τ_{yx}^{mem} (dotted magenta), and τ_{yx}^{res} (dashed green), and the corresponding phase averages are given in the caption. We see that $\bar{\tau}_{yx}^{\text{VE}}$ is positive (dot-dashed black line, $\bar{\tau}_{yx}^{\text{VE}}=0.013$), which corresponds to a negative tangential stress acting on the mucus, and that this non-zero phase average is mainly due to the memory term ($\bar{\tau}_{yx}^{\text{mem}}=0.0127$). Thus, it is the memory terms in the viscoelastic constitutive relations (2.2) that causes a non-symmetrical stress distribution, breaking the symmetry of the cellular flow pattern observed in the Newtonian limit. We point out that τ_{yx}^{mem} contains time derivatives stemming from (2.2a) and (2.2c), due to the nonlinear terms in the upper-convected derivative.

5.2. Additional role of shear-thinning

It has been demonstrated by Jory *et al.* (2022) that mucus also exhibits a shear-thinning behavior over a considerable range of strain rate $\dot{\gamma}$, which we quantify via the second principal invariant of the deformation tensor \mathbf{D} :

$$\dot{\gamma} = D_{xx}D_{yy} - D_{xy}D_{yx}, \quad \mathbf{D} = D_{ij} = \frac{1}{2} \{ \partial_{x_i} u_j + \partial_{x_j} u_i \}, \quad (5.2)$$

$$x_i = [x, y]^T, \quad u_i = [u, v]^T, \quad (5.3)$$

where we have used Einstein notation. In figure 8a, we have reproduced the steady-state rheometry data (open circles) measured by Jory *et al.* (2022) via a viscosity μ versus $\dot{\gamma}$ plot. The green shaded region marks the range of $\dot{\gamma}$ observed in one of our MCC computations from section 5.1, for which figure 8b represents streamlines and $\dot{\gamma}$ contours. Based on these data alone, one would expect the shear-thinning nature of mucus to greatly affect MCC in our configuration. However, the extent of this effect depends on how shear-thinning enters the constitutive relations for the viscous stresses.

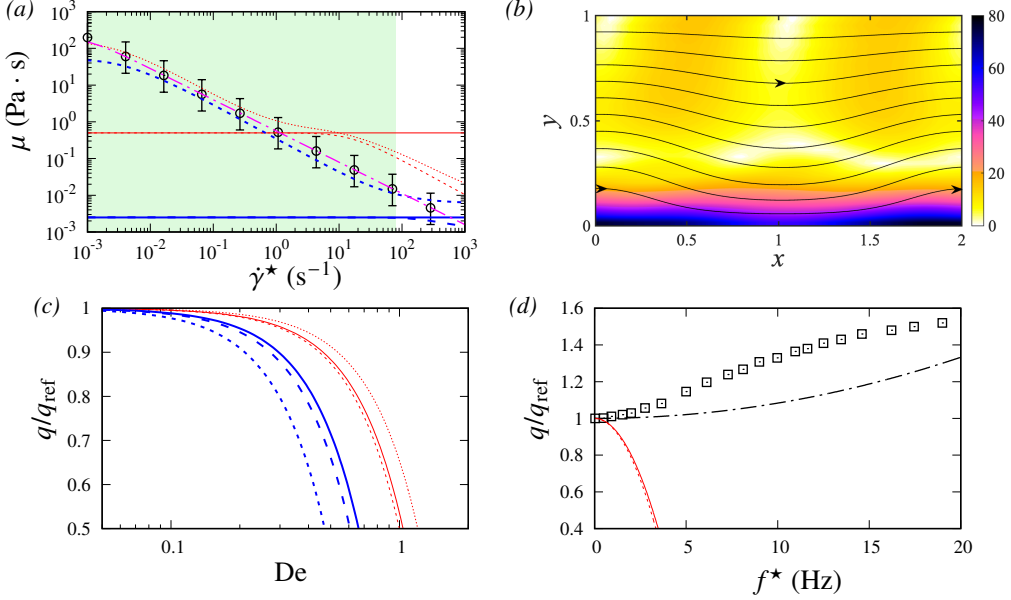


Figure 8: Additional effect of shear-thinning on MCC. (a) Steady-state stress-strain responses for constitutive models according to table 2. Total mucus viscosity μ versus strain rate $\dot{\gamma}^*$ (5.2). Thin red curves: HBE-5wt%, thick blue curves: HBE-2wt%. Circles: experimental data of Jory *et al.* (2022), dot-dashed: Carreau-Yasuda model (5.6) with $\lambda=1 \times 10^3$ s, $\mu_0=200$ Pa·s, $\mu_\infty=0$, $m=2$, $n=0.15$, solid: Oldroyd-B, dashed: single-mode Giesekus, dotted: 5-mode Giesekus; (b) streamlines and contours of $\dot{\gamma}^*$ for parameters according to figure 3b; (c) corresponding low-De predictions of MCC flow rate for the three viscoelastic models from panel (a); (d) corresponding MCC flow rate for Carreau-Yasuda model (5.6) from panel a. Squares: DNS, dot-dashed: low- λ asymptotic solution, dashed/solid: Giesekus/Oldroyd-B predictions from panel (c).

422 Vasquez *et al.* (2016) have shown that a five-mode Giesekus model is required to capture
 423 quantitatively both the viscoelastic and shear-thinning behavior of mucus:

$$424 \quad \boldsymbol{\tau} = \sum_{m=1}^N \boldsymbol{\tau}_m, \quad \boldsymbol{\tau}_m + \text{De}_m \left[\nabla \boldsymbol{\tau}_m + \alpha_m \frac{1 - \beta_m}{\beta_m} \boldsymbol{\tau}_m \cdot \boldsymbol{\tau}_m \right] = \frac{1 - \beta_m}{\beta_m} \mathbf{D}, \quad (5.4a)$$

$$425 \quad \nabla \boldsymbol{\tau}_m = \partial_t \boldsymbol{\tau}_m + \mathbf{u} \cdot \nabla \boldsymbol{\tau}_m - (\nabla \mathbf{u})^T \cdot \boldsymbol{\tau}_m - \boldsymbol{\tau}_m \cdot \nabla \mathbf{u}, \quad (5.4b)$$

426 where N is the number of modes ($N=5$ for the 5-mode model), m is the mode index,
 427 $\text{De}_m = \lambda_m \omega^*$, $\beta_m = \mu_s / (\mu_s + \mu_p^{(m)})$, and $\alpha_m \leq 0.5$ denotes the so-called mobility parameter.
 428 Here, we have used Gibbs notation for brevity, and the decoration ∇ denotes the upper-
 429 convected derivative. For $N=1$ and $\alpha=0$, (5.4) reduces to the (single-mode) Oldroyd-B model
 430 (2.2), which is devoid of shear-thinning.

431 The shear-thinning property of mucus is imparted by the α_m term in (5.4). From the
 432 quadratic nature of this term, it is straightforward to show that it intervenes only at $\mathcal{O}(a^4)$
 433 in a low-amplitude expansion of the governing equations. Thus, our result in (4.9) remains
 434 unaltered when using a (single-mode) Giesekus constitutive model (5.4). The equivalence
 435 of the Oldroyd-B and Giesekus models in the low- a limit has been demonstrated by Lauga
 436 (2007), and we have confirmed it for our current configuration. As our low-amplitude
 437 predictions based on (4.9) in figure 5 (dashed curves there) agree very well with our DNS
 438 (symbols in figure 5) for the HBE-2 wt% (circles) and HBE-5 wt% (diamonds) mucus in the
 439 MCC frequency range, we may conclude that these results are unaffected by shear-thinning.

HBE	N	$[\beta'_1, \dots, \beta'_N]$	$[\lambda_1, \dots, \lambda_N]$ (s)	$[\alpha_1, \dots, \alpha_N]$
5wt%	5	$[64, 32, 3.2, 0.3, 0.03] \times 10^{-2}$	$[521, 201, 51, 0.06, 0.03]$	$[0.5, 0.5, 0.5, 0.3, 0.2]$
2wt%	5	$[9994, 2.2, 0.2, 0.2] \times 10^{-4}$	$[1453, 1.85, 1.2, 0.91, 10^{-5}]$	$[0.01, 0.1, 0.1, 0.5, 0.5]$
5wt%	1	[0.998]	[0.052]	[0.5]
2wt%	1	[0.6]	[0.003]	[0.5]
5wt%	1	[0.998]	[0.052]	[0]
2wt%	1	[0.6]	[0.003]	[0]

Table 2: Parameters according to (5.4) for the constitutive models underlying curves in figure 8c, i.e. 5-mode Giesekus, single-mode Giesekus, and Oldroyd-B models. The solvent viscosity is $\mu_s = 1 \times 10^{-3}$ Pa · s. All other parameters have been fitted to the complex modulus data of Hill *et al.* (2014), listed in table 1, and the shear-thinning rheology measured by Jory *et al.* (2022). The steady-state stress-strain responses of the three models are plotted in figure 8a.

440 We now consider the low-De limit. For this, we assume $\lambda_1 \geq \lambda_m$ in (5.4), and define
 441 $\text{De}_m = \Pi_m \text{De}$, where $\text{De} = \lambda_1 \omega^*$ and $\Pi_m = \lambda_m / \lambda_1$. This allows us to apply the regular perturba-
 442 tion expansion (4.2) using $\epsilon = \text{De}$. In the limit $\zeta = 0$, we obtain:

$$443 \quad \left. \frac{q}{q_{\text{ref}}} \right|_{\zeta=0} = -\text{De}^2 \sum_{m=1}^N \beta'_m \Pi_m^2 \frac{(S^2 + 6k\phi SC)}{(S + 2k\phi C)^2} + O(\text{De}^3), \quad (5.5)$$

444 where $\beta'_m = \mu_p^{(m)} / (\mu_s + \sum_{m=1}^N \mu_p^{(m)})$. In the limit $N=1$, we obtain $\beta'_1 = 1 - \beta_1$, and (5.5) reduces
 445 to our solution (4.4) obtained from the Oldroyd-B model (2.2). This is because the mobility
 446 parameters α_m do not enter (5.5), and, thus, shear-thinning plays no role, at least in the
 447 $\zeta=0$ limit, which was considered in figures 6 and 7. The α_m do appear in the full analytical
 448 solution ($\zeta=1$), which is too long to reproduce here. Instead, we plot this solution in figure
 449 8c for parameters corresponding to HBE-2 wt% (thin blue curves) and HBE-5 wt% (thick
 450 red curves) mucus.

451 All curves in figure 8c represent low-De predictions of q/q_N for $\zeta=1$. Dotted and dashed
 452 curves correspond to the Giesekus model (5.4) with $N=5$ and $N=1$, respectively, and solid
 453 curves to the Oldroyd-B model (2.2). The associated rheological parameters, β'_m , λ_m , and
 454 α_m , are given in table 2. These were fitted to recover the complex moduli G' and G'' in table
 455 1 based on (3.1), and, in the case of the Giesekus model, additionally to recover the shear-
 456 thinning rheology measured by Jory *et al.* (2022), based on the *material functions* given in
 457 Bird *et al.* (1987). The steady-state μ versus $\dot{\gamma}$ relationships underlying the different curves
 458 in figure 8c are plotted in figure 8a using the same line styles. Whereas the total viscosity
 459 μ is constant for the Oldroyd-B model (solid curves in figure 8a), the 5-mode Giesekus
 460 model (dotted curves in figure 8a) reproduces the shear-thinning behavior displayed by the
 461 experimental data (open circles).

462 Comparing the dashed and solid curves in figure 8c, we may conclude that the shear-
 463 thinning nature of mucus does not significantly affect the MCC flow rate in the low-De limit.
 464 Thus, all our conclusions based on (4.3) in section (5.1) remain valid. This is due to the way
 465 in which shear-thinning enters the problem via (5.4), i.e. the α_m term there is multiplied by
 466 De_m . As a result, the shear-thinning property of mucus is enslaved to its viscoelastic nature.
 467 In that sense, the former effect is subordinate to the latter. In other words, shear-thinning
 468 only enters our MCC problem via viscoelasticity-induced perturbations of the flow field.

469 Of course, a final account of the role of shear-thinning requires full DNS based on the
 470 Giesekus model (5.4). In particular, this concerns the intermediate mucus types in figure 5,
 471 where neither the low- a nor the low- De predictions accurately follow the DNS within the
 472 MCC frequency range. Such new DNS are outside the scope of our manuscript, as they would
 473 require substantially modifying the Basilisk solver to implement the Giesekus model (5.4).

474 To emphasize the particular way in which shear-thinning enters the Giesekus model, we
 475 compare our results with predictions based on a generalized Newtonian description for a
 476 shear-thinning fluid. In this case, the mucus is purely viscous, and we choose the Carreau-
 477 Yasuda model (Carreau *et al.* 1979) to describe its viscosity:

$$478 \quad \mu(\dot{\gamma}) = \mu_{\infty} + (\mu_0 - \mu_{\infty}) \left[1 + (\lambda \dot{\gamma})^l \right]^{\frac{n-1}{l}}, \quad (5.6)$$

479 where the relaxation time λ is not to be confused with an elastic relaxation time, μ_0 and μ_{∞}
 480 are the low- and infinite-strain-rate limits, and $l > 0$ and $n < 1$ are adjustable parameters. We
 481 set $\mu_{\infty} = 0$ and $l = 2$, and we fit λ , μ_0 , and n to the experiments of Jory *et al.* (2022), which
 482 yields the dot-dashed magenta curve in figure 8a.

483 Figure 8d compares predictions of the MCC flow rate q based on (5.6), as obtained
 484 from our own DNS (open squares) and a low- λ asymptotic solution (dot-dot-dashed black
 485 curve), with our low- De predictions based on the 5-mode Giesekus (dot-dashed red curve)
 486 and Oldroyd-B (solid red curve) models. In the case of the Giesekus model, shear-thinning
 487 amplifies (very slightly) the flow rate reduction caused by viscoelasticity. By contrast, an
 488 increase in flow rate is observed in the case of the Carreau-Yasuda model ($q/q_{\text{ref}} > 1$). At first
 489 sight, the latter observation seems to contradict the conclusions of Chatelin *et al.* (2017),
 490 who reported conditions where the MCC velocity is reduced due to shear-thinning. However,
 491 these authors also found that the shear-thinning effect is highly non-monotonic, and their
 492 figure 3 exhibits regions of parameter space where the MCC velocity is increased.

493 6. Conclusion

494 We have studied analytically and numerically the effect of viscoelasticity on MCC in a
 495 continuous force-free mucus layer, where momentum transfer from the beating cilia is
 496 modelled via the experimentally-validated Navier-slip moving-carpet boundary condition
 497 of Bottier *et al.* (2017a). In our continuum model, we have represented physiologically
 498 realistic conditions by appropriately choosing the mucus rheology (healthy and diseased
 499 conditions), cilia kinematics, and cilia density (which controls the slip length), based on
 500 literature data. We find that viscoelasticity can reduce the MCC flow rate by as much as 30%
 501 versus the Newtonian limit, under conditions representative of cystic fibrosis (CF), whereas
 502 no significant reduction is observed under healthy conditions. Moreover, the observed flow
 503 rate reduction is highly sensitive to the slip length and the cilia beat amplitude (CBA).

504 Translating the data reported in this study into dimensional terms, our calculations predict
 505 a 90% reduction of the MCC flow rate under CF conditions versus a healthy configuration,
 506 i.e. the average mucus velocity drops from 24–61 $\mu\text{m/s}$ for healthy mucus ($a^* = 5\text{--}8 \mu\text{m}$, HBE-
 507 2wt%) to 1.7 $\mu\text{m/s}$ for CF mucus ($a^* = 1.6 \mu\text{m}$, HBE-5wt%). This is a result of two effects
 508 associated with respiratory illnesses: reduced CBA and increased viscoelasticity. The role of
 509 CBA is both direct (via the imparted mucus velocity) and indirect (via viscoelasticity).

510 Thus, accurately predicting the effect of diseased conditions on CBA is an important
 511 modelling task. For example, in the case of CF, the PCL layer is depleted and so the cilia
 512 beat far into the viscoelastic mucus, reducing the CBA. Predicting this requires modelling
 513 the retro-action of mucus rheology on cilia kinematics. Very few studies have accounted

514 for such a retro-action. A promising route is the traction-layer model of [Smith *et al.* \(2007\)](#),
 515 which could be extended to account for a nonlinear viscoelastic rheology in the mucus layer.

516 Our analytical solution in the low-amplitude limit, which extends the theory of [Lauga](#)
 517 [\(2007\)](#) by accounting for wall slip, accurately predicts MCC flow rates versus our DNS for
 518 healthy and unhealthy conditions. Such low-cost predictions could be highly useful in large-
 519 scale models of the pulmonary network ([Filoche *et al.* 2015](#)). On the other hand, our low-De
 520 asymptotic solution has allowed us to elucidate the mechanism of viscoelasticity-induced
 521 MCC flow rate reduction. We find that memory effects associated with the metachronal
 522 wave are responsible for this, explaining why earlier studies that did not account for
 523 metachronicity ([Vasquez *et al.* 2016](#); [Ortín 2020](#)) did not observe any effect of rheology
 524 on the net mucus flow rate. In the case of microorganisms swimming in an unbounded fluid
 525 domain and modelled via Taylor’s swimming sheet approach, [Riley & Lauga \(2015\)](#) have
 526 shown that a waveform consisting of two superimposed counter-travelling waves can lead
 527 to a viscoelasticity-induced increase in the swimming speed. However, such a waveform
 528 has not been reported in the context of MCC. Our analytical asymptotic solutions in
 529 the low-amplitude and low-De limits are not significantly affected by the shear-thinning
 530 nature of mucus, which we have represented via a multi-mode Giesekus model following
 531 [Vasquez *et al.* \(2016\)](#); [Sedaghat *et al.* \(2022\)](#). This is because shear-thinning enters this model
 532 via a quadratic stress term that is enslaved to viscoelasticity. As a result, all our conclusions
 533 based on the Oldroyd-B model remain valid when the additional effect of shear-thinning is
 534 accounted for.

535 Our continuum model can be extended in several ways. Firstly, the effect of an adjacent gas
 536 flow can be incorporated, in order to study the role of viscoelasticity in cough-induced
 537 clearance ([Modaresi & Shirani 2022](#)). Secondly, our model can be adapted to account
 538 for altered metachronicity, either due to gaps in the cilia carpet ([Loiseau *et al.* 2020](#);
 539 [Choudhury *et al.* 2021](#)) or due to ciliary dyskinesia. Thirdly, the model can be modified
 540 to account for mucus secretion and occlusion in axisymmetric configurations ([Halpern *et al.*](#)
 541 [2010](#); [Romano *et al.* 2021](#)). Finally, DNS based on the multi-mode Giesekus model would
 542 allow us to elucidate the role of shear-thinning for arbitrary CBA and De. For this, the
 543 `Basilisk` solver needs to be significantly modified.

544 **Acknowledgements.** The authors thank the anonymous referees for their suggestions and for checking
 545 several of our derivations.

546 **Funding.** The authors gratefully acknowledge funding provided by Labex LaSIPS at Université Paris-Saclay
 547 via project *mucusFILM*.

548 **Declaration of interests.** The authors report no conflict of interest.

549 **Author ORCIDs.** A. Choudhury, <https://orcid.org/0000-0001-9814-5483>; M. Filoche, <https://orcid.org/0000-0001-8637-3016>; N.M. Ribe, <https://orcid.org/0000-0003-0584-888X>; N. Grenier, <https://orcid.org/0000-0001-5436-7041>; G.F. Dietze, <https://orcid.org/0000-0003-1495-5505>

552 Appendix A. Expressions intervening in the low-De solution (4.3)

553 The coefficients A_i , B_i , C_i , and D_i appearing in (4.3a) are given by:

$$554 \quad A_1 = -\frac{a}{S + 2k\phi C}, \quad B_1 = \frac{ae^{-k} \sinh(k)}{k(S + 2k\phi C)}, \quad C_1 = -A_1, \quad D_1 = B_1 e^{2k}, \quad (\text{A } 1)$$

$$555 \quad A_2 = \frac{1}{2} a^2 k, \quad (\text{A } 2)$$

$$556 \quad A_3 = \frac{a^2 k'}{4(S' + 2k'\phi C')}, \quad B_3 = -\frac{a^2(1 - e^{-2k'})}{8(S' + 2k'\phi C')}, \quad C_3 = -A_3, \quad D_3 = B_3 e^{2k'}, \quad (\text{A } 3)$$

557 where we have introduced $S=\sinh(2k) - 2k$, $C=\cosh(2k) - 1$, $S'=\sinh(2k') - 2k'$, and
 558 $C'=\cosh(2k') - 1$, with $k'=2k$. The homogenous and particular solutions $\Psi_H(x, y, t)$ and
 559 $\Psi_P(x, y, t)$ in (4.3c) are:

$$\begin{aligned}
 560 \quad \Psi_H(x, y, t) &= A_{10}y + B_{10}y^2 \\
 561 \quad &+ \sum_{n=1}^6 \left\{ \cos(n\theta) \left(e^{nky} (A_{1n} + B_{1n}ky) + e^{-nky} (C_{1n} + D_{1n}ky) \right) \right\}, \quad (\text{A } 4) \\
 562 \quad \Psi_P(x, y, t) &= \sum_{n=1,2}^3 \sum_{p=0}^3 \left(e^{2nky} I_{pn}y^p + e^{-2nky} J_{pn}y^p \right) \\
 563 \quad &+ \sum_{n=1,2}^5 \sum_{p=2}^5 \left\{ \cos(n\theta) \left(e^{nky} Y_{pn}y^p + e^{-nky} Z_{pn}y^p \right) \right\} \\
 564 \quad &+ \cos(\theta) \sum_{n=1,2}^3 \sum_{p=0}^3 \left(e^{(2n+1)ky} Q_{pn}y^p + e^{-(2n+1)ky} R_{pn}y^p \right) \\
 565 \quad &+ \cos(2\theta) \sum_{n=0,2,3}^3 \sum_{p=0}^3 \left(e^{2nky} K_{pn}y^p + e^{-2nky} L_{pn}y^p \right) \\
 566 \quad &+ \cos(3\theta) \sum_{n=0,2}^3 \sum_{p=0}^3 \left(e^{(2n+1)ky} E_{pn}y^p + e^{-(2n+1)ky} F_{pn}y^p \right) \\
 567 \quad &+ \cos(4\theta) \sum_{p=0}^3 \left(e^{2ky} M_p y^p + e^{-2ky} N_p y^p + X_p y^p \right) \\
 568 \quad &+ \cos(5\theta) \sum_{n=0,1}^3 \sum_{p=0}^3 \left(e^{(2n+1)ky} G_{pn}y^p + e^{-(2n+1)ky} H_{pn}y^p \right) \\
 569 \quad &+ \cos(6\theta) \sum_{p=0}^3 \left(e^{2ky} O_p y^p + e^{-2ky} P_p y^p \right), \quad (\text{A } 5) \\
 570
 \end{aligned}$$

571 where $\theta=kx + t$ and $L_{p0} = 0$. The constants A_{ij} , B_{ij} , C_{ij} , \dots , and M_i , N_i , O_i , P_i , and X_i can
 572 be obtained in a straightforward manner via the method of undetermined coefficients. The
 573 fully substituted forms of Ψ_H and Ψ_P are given in the supplementary Mathematica notebook.

574 **Appendix B. Coefficients intervening in the low-amplitude solution (4.8)**

575 The coefficients contained in (4.8) are given by:

$$\begin{aligned}
 576 \quad I_0 &= \frac{(1 - \beta)\text{De}^2 k (2k + e^{-2k} - 1)}{4 (1 + \text{De}^2) (S + 2k\phi C)^2}, \quad I_1 = -\frac{(1 - \beta)\text{De}^2 (e^{2k} - 1) k (e^{-2k} (4k - 1) + e^{-4k})}{8 (1 + \text{De}^2) (S + 2k\phi C)^2}, \\
 577 \quad I_2 &= \frac{(1 - \beta)\text{De}^2 e^{-4k} (e^{2k} - 1)^2 k^2}{8 (1 + \text{De}^2) (S + 2k\phi C)^2}, \quad J_0 = -\frac{(1 - \beta)\text{De}^2 k (2k - e^{2k} + 1)}{4 (1 + \text{De}^2) (S + 2k\phi C)^2} \\
 578 \quad J_1 &= -\frac{(1 - \beta)\text{De}^2 (e^{2k} - 1) k (4k - e^{2k} + 1)}{8 (1 + \text{De}^2) (S + 2k\phi C)^2}, \quad J_2 = -\frac{(1 - \beta)\text{De}^2 (e^{2k} - 1)^2 k^2}{8 (1 + \text{De}^2) (S + 2k\phi C)^2}, \quad (\text{B } 1) \\
 579
 \end{aligned}$$

$$\begin{aligned}
580 \quad K_1 &= \frac{1}{2} e^{-2k} \left[-8k\phi(J_0k + J_1(k-1)) - 4J_2(2(k-2)k+1)\phi + e^{2k} \left(4J_0k(2k\phi+1) \right. \right. \\
581 \quad &\quad \left. \left. - 2J_1(4k\phi+1) + 4J_2\phi + I_0k(8k\phi-4) + 8I_1k\phi + k + 4I_2\phi - 2I_1 \right) \right. \\
582 \quad &\quad \left. - 4e^{4k} \left(2k(I_0k + I_1(k+1)) + I_2(2k(k+2)+1) \right) \phi \right], \\
583 \quad K_2 &= e^{-2k} \left[2k \left(-(J_0 + J_1 + J_2)k + J_1 + 2J_2 \right) - J_2 - e^{4k} \left(2k(I_0k + I_1(k+1)) \right. \right. \\
584 \quad &\quad \left. \left. + I_2(2k(k+2)+1) \right) \right], \tag{B 2} \\
585
\end{aligned}$$

586 where we have once again used $S=\sinh(2k) - 2k$ and $C=\cosh(2k) - 1$.

REFERENCES

- 587 ANGELES, V., GODÍNEZ, F. A., PUENTE-VELAZQUEZ, J. A., MENDEZ-ROJANO, R., LAUGA, E. & ZENIT, R. 2021
588 Front-back asymmetry controls the impact of viscoelasticity on helical swimming. *Phys. Rev. Fluids*
589 **6**, 043102.
- 590 BELL, J. B., COLELLA, P. & GLAZ, H. M. 1989 A second-order projection method for the incompressible
591 Navier-Stokes equations. *Journal of Computational Physics* **85**, 257–283.
- 592 BIRD, R. B., ARMSTRONG, R. C. & HASSAGER, O. 1987 *Dynamics of polymeric liquids. Vol. 1: Fluid*
593 *mechanics*. John Wiley and Sons Inc., New York, NY.
- 594 BLAKE, J. 1973 Mucus flows. *Mathematical Biosciences* **17** (3-4), 301–313.
- 595 BOTTIER, M., BLANCHON, S., PELLE, G., BEQUIGNON, E., ISABEY, D., COSTE, A. & OTHERS 2017a A new
596 index for characterizing micro-bead motion in a flow induced by ciliary beating: Part I, experimental
597 analysis. *PLoS Computational Biology* **13** (7), e1005605.
- 598 BOTTIER, M., DELGADO, L., SHUTTLEWORTH, M. K., CASSIDY, D. M., CRICHTON, M. L., GALLANT, S. &
599 OTHERS 2022 Characterization of ciliary function in bronchiectasis (embarc-bridge study). In *A62.*
600 *Cystic Fibrosis and Non-CF Bronchiectasis: Mechanistic Insights*, p. A2000. American Thoracic
601 Society.
- 602 BOTTIER, M., PEÑA FERNÁNDEZ, M., PELLE, G., ISABEY, D., LOUIS, B., GROTBORG, J. B. & OTHERS 2017b
603 A new index for characterizing micro-bead motion in a flow induced by ciliary beating: Part II,
604 modeling. *PLoS computational biology* **13** (7), e1005552.
- 605 BUTTON, B., CAI, L.-H., EHRE, C., KESIMER, M., HILL, D. B., SHEEHAN, J. K., BOUCHER, R. C. & RUBINSTEIN,
606 M. 2012 A periciliary brush promotes the lung health by separating the mucus layer from airway
607 epithelia. *Science* **337** (6097), 937–941.
- 608 CARREAU, P.J., KEE, D DE & DAROUX, M 1979 An analysis of the viscous behaviour of polymeric solutions.
609 *The Canadian Journal of Chemical Engineering* **57** (2), 135–140.
- 610 CHATELIN, R., ANNE-ARCHARD, D., MURRIS-ESPIN, M., THIRIET, M. & PONCET, P. 2017 Numerical
611 and experimental investigation of mucociliary clearance breakdown in cystic fibrosis. *Journal of*
612 *biomechanics* **53**, 56–63.
- 613 CHOUDHURY, A., DEY, M., DIXIT, H. N. & FENG, J. J. 2021 Tear-film breakup: The role of membrane-
614 associated mucin polymers. *Phys. Rev. E* **103**, 013108.
- 615 FAHY, J. V. & DICKEY, B. F. 2010 Airway mucus function and dysfunction. *New England journal of medicine*
616 **363** (23), 2233–2247.
- 617 FATTAL, R. & KUPFERMAN, R. 2005 Time-dependent simulation of viscoelastic flows at high weissenberg
618 number using the log-conformation representation. *Journal of Non-Newtonian Fluid Mechanics*
619 **126** (12), 23–37.
- 620 FILOCHE, M., TAI, C.-F. & GROTBORG, J. B. 2015 Three-dimensional model of surfactant replacement
621 therapy. *Proc. Natl. Acad. Sci. U.S.A.* **112** (30), 9287–9292.
- 622 FULFORD, G. R. & BLAKE, J. R. 1986 Muco-ciliary transport in the lung. *Journal of theoretical Biology*
623 **121** (4), 381–402.
- 624 GROTBORG, J. B. 2021 *Biofluid Mechanics: Analysis and Applications*. Cambridge University Press.

- 625 GUO, H. & KANSO, E. 2017 A computational study of mucociliary transport in healthy and diseased
626 environments. *European Journal of Computational Mechanics* **26** (1-2), 4–30.
- 627 HALPERN, D., FUJIOKA, H. & GROTEBERG, J. B. 2010 The effect of viscoelasticity on the stability of a
628 pulmonary airway liquid layer. *Physics of Fluids* **22**, 011901.
- 629 HILL, D. B., VASQUEZ, P. A., MELLNIK, J., MCKINLEY, S. A., VOSE, A., MU, F. & OTHERS 2014 A biophysical
630 basis for mucus solids concentration as a candidate biomarker for airways disease. *PLoS one* **9** (2),
631 e87681.
- 632 JORY, M., DONNARUMMA, D., BLANC, C., BELLOUMA, K., FORT, A., VACHIER, I. & OTHERS 2022 Mucus from
633 human bronchial epithelial cultures: rheology and adhesion across length scales. *Interface Focus*
634 **12** (6), 20220028.
- 635 LAUGA, E. 2007 Propulsion in a viscoelastic fluid. *Physics of Fluids* **19** (8), 083104.
- 636 LAUGA, E. 2020 *The fluid dynamics of cell motility*, , vol. 62. Cambridge University Press.
- 637 LEVY, R., HILL, D. B., FOREST, M. G. & GROTEBERG, J. B. 2014 Pulmonary fluid flow challenges for
638 experimental and mathematical modeling. *Integrative and Comparative Biology* **54** (6), 985–1000.
- 639 LOISEAU, E., GSELL, S., NOMMICK, A., JOMARD, C., GRAS, D., CHANEZ, P. & OTHERS 2020 Active mucus–
640 cilia hydrodynamic coupling drives self-organization of human bronchial epithelium. *Nature Physics*
641 **16** (11), 1158–1164.
- 642 LÓPEZ-HERRERA, J. M., POPINET, S. & CASTREJÓN-PITA, A. 2019 An adaptive solver for viscoelastic
643 incompressible two-phase problems applied to the study of the splashing of weakly viscoelastic
644 droplets. *Journal of Non-Newtonian Fluid Mechanics* **264**, 144–158.
- 645 MAN, Y. & LAUGA, E. 2015 Phase-separation models for swimming enhancement in complex fluids. *Physical*
646 *Review E* **92** (2), 023004.
- 647 MITRAN, S. M. 2007 Metachronal wave formation in a model of pulmonary cilia. *Computers & structures*
648 **85** (11-14), 763–774.
- 649 MITRAN, S. M., FOREST, M. G., YAO, L., LINDLEY, B. & HILL, D. B. 2008 Extensions of the ferry shear wave
650 model for active linear and nonlinear microrheology. *Journal of non-Newtonian fluid mechanics*
651 **154** (2-3), 120–135.
- 652 MODARESI, M. A. & SHIRANI, E. 2022 Effects of continuous and discrete boundary conditions on the
653 movement of upper-convected maxwell and Newtonian mucus layers in coughing and sneezing. *The*
654 *European Physical Journal Plus* **137** (7), 846.
- 655 ORTÍN, J. 2020 Stokes layers in oscillatory flows of viscoelastic fluids. *Philosophical Transactions of the*
656 *Royal Society A* **378** (2174), 20190521.
- 657 POPINET, S. 2015 A quadtree-adaptive multigrid solver for the serre-green-naghdi equations. *Journal of*
658 *Computational Physics* **302**, 336–358.
- 659 POPINET, S. & COLLABORATORS 2013–2020 Basilisk. <http://basilisk.fr>.
- 660 RILEY, E. E. & LAUGA, E. 2015 Small-amplitude swimmers can self-propel faster in viscoelastic fluids.
661 *Journal of theoretical biology* **382**, 345–355.
- 662 ROMANO, F., MURADOGLU, M., FUJIOKA, H. & GROTEBERG, J. B. 2021 The effect of viscoelasticity in an
663 airway closure model. *Journal of Fluid Mechanics* **913**, A31.
- 664 SEDAGHAT, M. H., BEHNIA & M., ABOUALI, O. 2023 Nanoparticle diffusion in respiratory mucus influenced
665 by mucociliary clearance: A review of mathematical modeling. *Journal of Aerosol Medicine and*
666 *Pulmonary Drug Delivery* .
- 667 SEDAGHAT, M. H., FARNOUD, A., SCHMID, O. & ABOUALI, O. 2022 Nonlinear simulation of mucociliary
668 clearance: A three-dimensional study. *Journal of Non-Newtonian Fluid Mechanics* **300**, 104727.
- 669 SEDAGHAT, M. H., SHAHMARDAN, M. M., NOROUZI, M. & HEYDARI, M. 2016 Effect of cilia beat frequency
670 on muco-ciliary clearance. *Journal of Biomedical Physics & Engineering* **6** (4), 265.
- 671 SIGINER, D. A. 2014 *Stability of non-linear constitutive formulations for viscoelastic fluids*. Springer.
- 672 SMITH, D. J., GAFFNEY, E. A. & BLAKE, J. R. 2007 A viscoelastic traction layer model of muco-ciliary
673 transport. *Bulletin of mathematical biology* **69** (1), 289–327.
- 674 SPAGNOLIE, S. E., ed. 2015 *Complex Fluids in Biological Systems - Experiment, Theory, and Computation*.
675 New York: Springer.
- 676 VANAKI, S. M., HOLMES, D., SAHA, S. C., CHEN, J., BROWN, R. J. & JAYATHILAKE, P. G. 2020 Muco-ciliary
677 clearance: A review of modelling techniques. *Journal of biomechanics* **99**, 109578.
- 678 VASQUEZ, P. A., JIN, Y., PALMER, E., HILL, D. & FOREST, M. G. 2016 Modeling and simulation of mucus
679 flow in human bronchial epithelial cell cultures–part I: Idealized axisymmetric swirling flow. *PLoS*
680 *Computational Biology* **12** (8), e1004872.